ACS APPLIED MATERIALS & INTERFACES
Research Article
www.acsami.org

Contrasting the Role of Mg and Ba Doping on the Microstructure and Thermoelectric Properties of p-Type $AgSbSe_2$

Zihang Liu,[†] Jing Shuai,[‡] Huiyuan Geng,[§] Jun Mao,[∥] Yan Feng,[⊥] Xu Zhao,[†] Xianfu Meng,[†] Ran He,[‡] Wei Cai,[*,†] and Jiehe Sui[*,†]

[†]National Key Laboratory for Precision Hot Processing of Metals and School of Materials Science and Engineering and [§]State Key Laboratory of Advanced Welding and Joining, Harbin Institute of Technology, Harbin 150001, China

[‡]Department of Physics and TcSUH and [∥]Department of Mechanical Engineering, University of Houston, Houston, Texas 77204, United States

[⊥]State Key Laboratory of Solidification Processing, Northwestern Polytechnical University, Xi'an 710072, China

Supporting Information

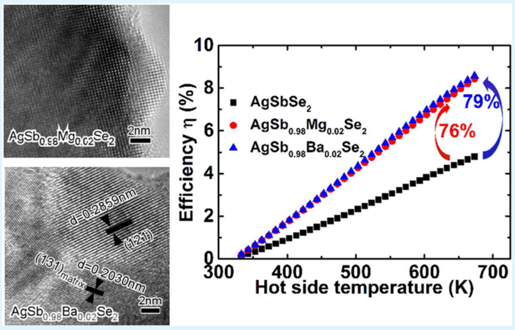

ABSTRACT: Microstructure has a critical influence on the mechanical and functional properties. For thermoelectric materials, deep understanding of the relationship of microstructure and thermoelectric properties will enable the rational optimization of the *ZT* value and efficiency. Herein, taking $AgSbSe_2$ as an example, we first report a different role of alkaline-earth metal ions (Mg^{2+} and Ba^{2+}) doping in the microstructure and thermoelectric properties of p-type $AgSbSe_2$. For Mg doping, it monotonously increases the carrier concentration and then reduces the electrical resistivity, leading to a substantially enhanced power factor in comparison to those of other dopant elements (Bi^{3+}, Pb^{2+}, Zn^{2+}, Na^{+}, and Cd^{2+}) in the $AgSbSe_2$ system. Meanwhile, the lattice thermal conductivity is gradually suppressed by point defects scattering. In contrast, the electrical resistivity first decreases and then slightly rises with the increased Ba-doping concentrations due to the presence of $BaSe_3$ nanoprecipitates, exhibiting a different variation tendency compared with the corresponding Mg-doped samples. More significantly, the total thermal conductivity is obviously reduced with the increased Ba-doping concentrations partially because of the strong scattering of medium and long wavelength phonons via the nanoprecipitates, consistent with the theoretical calculation and analysis. Collectively, *ZT* value ~1 at 673 K and calculated leg efficiency ~8.5% with T_c = 300 K and T_h = 673 K are obtained for both $AgSb_{0.98}Mg_{0.02}Se_2$ and $AgSb_{0.98}Ba_{0.02}Se_2$ samples.

KEYWORDS: *$AgSbSe_2$, alkaline-earth metal ions (M^{2+}) doping, nanoprecipitates, microstructure, thermoelectric properties, leg efficiency*

1. INTRODUCTION

Thermoelectric materials, which could directly and reversibly convert heat energy into electrical power and provide an alternative for power generation and refrigeration, have received worldwide interests in the past decades.[1−3] Normally, the conversion efficiency of thermoelectric materials is determined by the dimensionless thermoelectric figure of merit $ZT = S^2\sigma T/(\kappa_{lat} + \kappa_{ele})$, where S, σ, κ_{lat}, κ_{ele}, and T are the Seebeck coefficient, electrical conductivity, lattice thermal conductivity, electronic thermal conductivity, and the absolute temperature, respectively. As the fundamental material parameters (σ, S, and κ_{ele}) are interrelated and conflicting in a single compound, it is indeed challenging to noticeably improve the thermoelectric performance.[4,5] Recently, several effective strategies, including band engineering,[6−8] nanoscale second phase,[9−11] bulk nanostructuring,[12] and panoscopic approach,[13−15] have been successfully introduced and developed to enhance the thermoelectric performance. Alternatively, we can optimize the electrical transport properties and then improve the final *ZT* value in the thermoelectric materials with an intrinsically low thermal conductivity,[16] which may be associated with large unit cell and molecular weight,[17] complex crystal structure,[18,19] lone pair electrons,[20] ion liquid-like transport behavior,[21,22] or anharmonic bonding.[23]

Recently, cubic A−B−X_2 compounds[24−27] (where A = Cu, Ag, Au, or alkali metal; B = Sb or Bi; and X = S, Se, or Te) have drawn renewed attention as thermoelectric materials due to the intrinsically low thermal conductivity rising from the lone electron of the V group elements (Sb or Bi).[28] Among the materials system above, the $AgSbTe_2$ system has manifested high thermoelectric performance, *ZT*, above unity.[24,25] More importantly, $(GeTe)_{0.85}(AgSbTe_2)_{0.15}$ alloy, known as TAGS, had been successfully used in the early radioisotope thermoelectric generators since the 1950s.[2,4] However, Tellurium (Te)

Received: July 17, 2015
Accepted: October 5, 2015
Published: October 5, 2015

DOI: 10.1021/acsami.5b06492
ACS Appl. Mater. Interfaces 2015, 7, 23047−23055

is an extremely scarce element on the earth's crust, the earth abundance around 0.001 ppm much lower to that of gold (Au) ~0.004 ppm.[29] Because the abundance of selenium (Se) is 5000 times higher than that of Te, A−B−Se_2 compounds have been a hot scientific issue in recent years.[26,30−36] Typically, $AgSbSe_2$ and $AgBiSe_2$ exhibit the *ZT* values in excess of 1 in the mediate temperature range.[26,30,32,33,36] For $AgBiSe_2$, Nb^{5+} doping optimizes the carrier concentration and the maximum *ZT* value is around 1.[30] In addition, aliovalent halide ion doping, acting as an effective n-type dopant, markedly increases the electrical conductivity and enhances the thermoelectric performance, $ZT \sim 0.75$ at 810 K.[31] However, pristine $AgBiSe_2$ exhibits two phase transitions from α to β at 470 K and β to γ at 570 K,[30] which easily results in severe performance degradation and device failure in the practical application. In contrast, there is no phase transition from room temperature to 673 K for $AgSbSe_2$. Moreover, the maximum *ZT* value is around 1 by Bi^{3+}, Pb^{2+}, Zn^{2+}, Na^{+}, and Cd^{2+} doping[26,33−35] or tuning the Sb content.[36] For example, 2 mol % Zn^{2+} doping not only optimizes the carrier concentrations but also leads to the formation of ZnSe endotaxial second phase in the $AgSbSe_2$ matrix, resulting in a high $ZT \sim 1.1$ at 635 K.[33] Similarly, 1 mol % Na^{+} doping improves the power factor as the acceptor doping and simultaneously decreases the lattice thermal conductivity caused by the presence of Na-rich micro-precipitates and stacking faults, leading to the dramatic enhancement of thermoelectric performance.[35] To our knowledge, there are no related reports on the microstructure and thermoelectric properties using alkaline-earth metal ions (M^{2+}) doping in the $AgSbSe_2$ system, although upon M^{2+} doping significant enhancement of the thermoelectric performance can be achieved in the system of PbTe,[13,37,38] PbSe,[39] BiCuSeO,[40−42] etc.

Here, we report and compare the effect of alkaline-earth metal ion (Mg^{2+} and Ba^{2+}) doping on the microstructure and thermoelectric properties. Briefly, as Mg^{2+} has a substantial solid solubility in the Sb^{3+} sublattice of $AgSbSe_2$, the electrical and thermal transport properties is monotonously changed with increasing Mg-doping concentrations. Moreover, a higher average power factor is achieved for $AgSb_{0.98}Mg_{0.02}Se_2$ sample from 300 to 673 K in comparison with those of other dopant elements (Bi^{3+}, Pb^{2+}, Zn^{2+}, Na^{+}, and Cd^{2+}) in the $AgSbSe_2$ system.[26,33−35] In contrast, a high density of $BaSe_3$ nanoprecipitates can be observed for $AgSb_{0.98}Ba_{0.02}Se_2$ sample by transmission electron microscopy (TEM) and high-resolution transmission electron microscopy (HRTEM), partially contributing to the ultralow total thermal conductivity from 0.48 W m^{-1} K^{-1} at 300 K to 0.35 W m^{-1} K^{-1} at 673 K. Besides, the presence of nanoprecipitates also causes the abnormal transport behavior in comparison with comparable amounts of Mg-doped $AgSbSe_2$ samples. Finally, the maximum *ZT* values around unity and high calculated leg efficiency of about 8.5% are achieved in our work. This further confirms that $AgSbSe_2$ is a promising Te-free candidate for power generation in the medium temperature range.

2. EXPERIMENTAL SECTION

Appropriate amounts of Ag (99.99%), Sb (99.999%), Se (99.98%), Mg (99.99%), and Ba (99.9%) from Alfa Aesar were weighed according to the nominal composition and then sealed into carbon-coated silica tubes. The raw materials were slowly raised to 1023 at 200 K h^{-1}, kept for 8 h, and then quenched in water. The obtained products were crushed into powders by hand in a glovebox and then densified using spark plasma sintering at 723 K for 2 min under an axial compressive stress of 80 MPa.

X-ray diffraction (XRD) analysis was performed using a PANalytical multipurpose diffractometer with an X'celerator detector (PANalyticalX'Pert Pro). Scanning electron microscopy (SEM) and TEM studies were performed using a HELIOS NanoLab 600i, FEI, and a Tecnai G2 F30, FEI, respectively. Specimens used for TEM were identical with those in previous publications.[11,35] The cutted bars were used for simultaneous measurement of the electrical resistivity (ρ) and Seebeck coefficient (*S*) on a commercial system (ULVACZEM-3). It should be noted that there is a 3% error in the electrical conductivity, 5% error in the Seebeck coefficient, leading to the error of 10% for the power factor. The thermal conductivity was calculated from $\kappa = DC_pd$, where D, C_p, and d are the thermal diffusivity, heat capacity, and density, respectively. The thermal diffusivity coefficient (D) was measured with the coin sample using the laser flash diffusivity method in a Netzsch LFA457 (NETZSCH, LFA457, Germany), shown in Figure S1 of the Supporting Information. The specific heat capacity (Cp), shown in Figure S2 was measured on a differential scanning calorimetry thermal analyzer Netzsch DSC 404 C. The density (d) was present in the Table 1, which was determined using the Archimedes method. When considering the uncertainties for D, C_p, and d, the error for the thermal conductivity κ is estimated to be around 8%, resulting in the error of 13% for the final *ZT*. The Hall coefficient R_H at room temperature was measured using the PPMS (Physical Properties Measurement System, Quantum Design). The carrier concentration (n) was obtained by $n = 1/eR_H$ and the carrier mobility (μ) was calculated by $\sigma = e\mu n$, where e is the electronic charge and σ the electrical conductivity.

Table 1. List of Density, Carrier Concentration, Mobility, and Effective Mass for $AgSb_{1-x}Mg_xSe_2$ and for $AgSb_{1-x}Ba_xSe_2$ Samples

samples	density (g cm^{-3})	n (10^{19} cm^{-3})	μ (cm^2 V^{-1} S^{-1})	m^* (m_0)
$AgSbSe_2$	6.4	0.6	22.5	1.7
$AgSb_{0.99}Mg_{0.01}Se_2$	6.3	3.1	14.6	1.9
$AgSb_{0.98}Mg_{0.02}Se_2$	6.3	5.9	11.5	2.1
$AgSb_{0.96}Mg_{0.04}Se_2$	6.2	6.5	11	2.0
$AgSb_{0.99}Ba_{0.01}Se_2$	6.4	2.4	10.6	2.0
$AgSb_{0.98}Ba_{0.02}Se_2$	6.5	5	9.7	2.1
$AgSb_{0.96}Ba_{0.04}Se_2$	6.5	3.8	8.2	2.2

3. RESULTS AND DISCUSSION

Parts (a) and (b) of Figure 1 show the XRD patterns of $AgSb_{1-x}Mg_xSe_2$ and $AgSb_{1-x}Ba_xSe_2$ samples (x = 0, 0.01, 0.02, and 0.04), respectively. For all the Mg-doped samples, all the peaks exhibit good match with the $AgSbSe_2$ (PDF#12-0379) with the space group $Fm\overline{3}m$ without impurity phase within the detection limit of XRD spectrometer, even for $AgSb_{0.96}Mg_{0.04}Se_2$ sample. However, the second-phase $BaSe_3$ can be detected for $AgSb_{0.96}Ba_{0.04}Se_2$ sample in Figure S3, which could be further confirmed by TEM and HRTEM results discussed later. As shown in Figure 1c, the lattice parameters are monotonously decreased with the increased Mg-doping concentration due to the difference between the ionic radius of Mg^{2+} (0.65 Å) and Sb^{3+} (0.92 Å). In contrast, as Ba^{2+} (1.35 Å) has a larger ionic radius than that of Sb^{3+} (0.92 Å), the lattice parameters first linearly increase with Ba-doping concentration and then keep saturated between $AgSb_{0.98}Ba_{0.02}Se_2$ and $AgSb_{0.96}Ba_{0.04}Se_2$ sample. Therefore, these results reveal that Mg^{2+} has a larger solid solubility higher than 0.04, while the solubility limit of Ba^{2+} is around 0.02 in the $AgSbSe_2$ system,

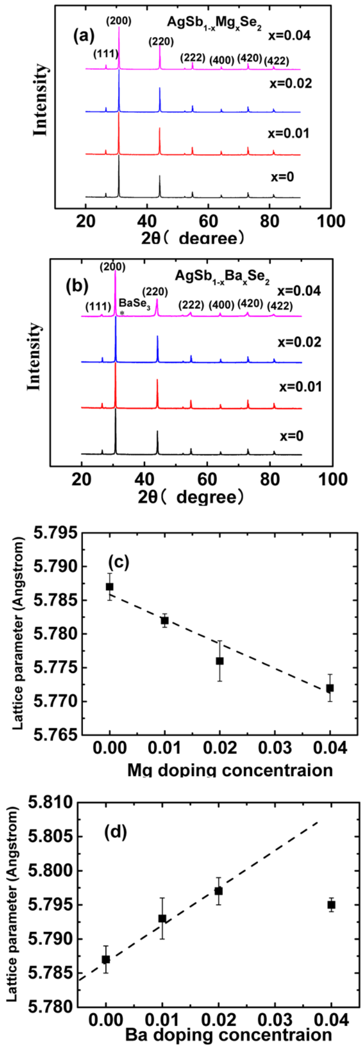

Figure 1. (a) XRD patterns for $AgSb_{1-x}Mg_xSe_2$ samples (x = 0, 0.01, 0.02, and 0.04). (b) XRD patterns for $AgSb_{1-x}Ba_xSe_2$ samples (x = 0, 0.01, 0.02, and 0.04). (c) Lattice parameter for $AgSb_{1-x}Mg_xSe_2$ samples. (d) Lattice parameter for $AgSb_{1-x}Ba_xSe_2$ samples. The dashed lines show the variation tendency for readability.

which would result in the different electron and phonon transport behavior.

To further differentiate the microstructure morphology of Mg-doping and Ba-doping samples, $AgSb_{0.98}Mg_{0.02}Se_2$ and $AgSb_{0.98}Ba_{0.02}Se_2$ samples were selected to investigate by using SEM and TEM. As shown inFigures S4 and S5, the element distribution determined by energy-dispersive X-ray spectroscopy indicates that all the elements are homogeneously distributed throughout the $AgSb_{0.98}Mg_{0.02}Se_2$ and $AgSb_{0.98}Ba_{0.02}Se_2$ samples on microscale level. Figure 2a shows the low-magnification TEM image of the $AgSb_{0.98}Mg_{0.02}Se_2$ sample and no impurity phase was found in the clear grain. The inset shows the corresponding electron diffraction pattern, which could be indexed into $AgSbSe_2$ with the space group $Fm\overline{3}m$ along the [111]C zone axis. As shown in Figure 2b, the HRTEM image indicates that even the nanoscale microstructure is uniform and homogeneous in the $AgSbSe_2$ matrix. In contrast, a high density of precipitates with the size ranging from 10 to 30 nm can be observed in the grain for the $AgSb_{0.98}Ba_{0.02}Se_2$ sample in Figure 2c. Figure 2d shows the representative HRTEM image of nanoprecipitates. The interplanar spaces of 0.2859 and 0.2030 nm corresponded with the (121) plane of $BaSe_3$ nanoprecipitate and (131) plane of the matrix, respectively. More importantly, the interfaces between the matrix and nanoprecipitates, typically semi-coherent or noncoherent, are beneficial in reducing the lattice thermal conductivity via strengthening the medium and long wavelength phonon scattering at the expense of the carrier mobility, which will be discussed later.

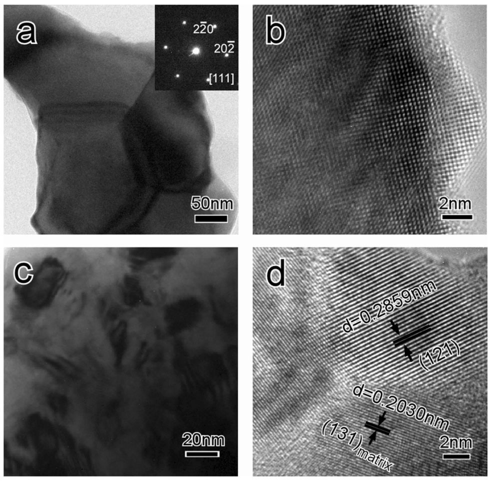

Figure 2. TEM images for $AgSb_{0.98}Mg_{0.02}Se_2$ and $AgSb_{0.98}Ba_{0.02}Se_2$ sample. (a) Low-magnification TEM image for the $AgSb_{0.98}Mg_{0.02}Se_2$ sample. Insert gives the corresponding SAED pattern along the [111] direction. (b) High-magnification TEM image for the $AgSb_{0.98}Mg_{0.02}Se_2$ sample. (c) Low-magnification TEM image for the $AgSb_{0.98}Ba_{0.02}Se_2$ sample. (d) High-magnification TEM image for the $AgSb_{0.98}Ba_{0.02}Se_2$ sample.

On the basis of simple valence electron counting, alkaline-earth metal ions (Mg^{2+} and Ba^{2+}) doping should act as electron acceptors to increase the hole carrier concentration of $AgSbSe_2$, as shown in Figure 3a. The carrier concentration of Mg-doping samples is gradually increased whereas the carrier concentration is first increased and then slightly dropped upon Ba doping

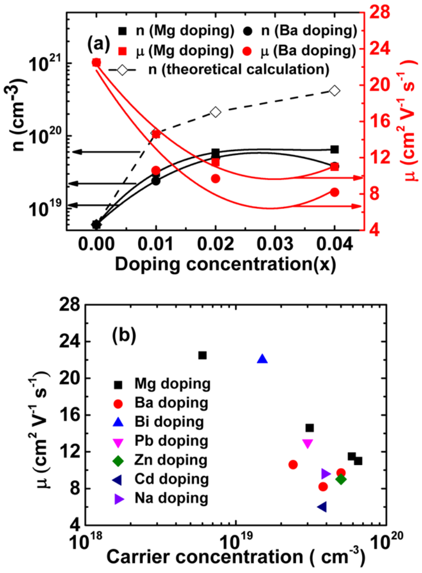

Figure 3. (a) Carrier concentration and mobility for Mg-doped and Ba-doped samples. (b) Carrier mobility as a function of carrier concentration, including Mg, Ba, Pb, Bi, Zn, Na, and Cd doping.

with increasing the doping concentration. This can be ascribed to the different solubility of Mg and Ba in the Sb sublattice of $AgSbSe_2$, consistent with the variation tendency of individual lattice parameters. In addition, Mg-doping samples have a higher carrier concentration than that of the corresponding Ba-doping samples, both of which were lower compared with the theoretical carrier concentration. Moreover, Mg doping could lead to a higher mobility than that of Ba doping, which may originate from the distinct microstructure. As shown in Figure 3b, the mobility of alkaline-earth metal ions (Mg^{2+} and Ba^{2+}) doping within the same carrier concentration range samples is comparable with previous reported results, including Pb^{2+}, Bi^{3+}, Zn^{2+}, Na^{+}, and Cd^{2+} doping.[26,33−35]

Parts (a) and (b) of Figure 4 show the temperature-dependent electrical resistivity of $AgSb_{1-x}Mg_xSe_2$ and $AgSb_{1-x}Ba_xSe_2$ samples, respectively. It is clear that the electrical resistivity decreases with increasing the Mg-doping concentration over the whole measured temperature range. Typically, the electrical resistivity at room temperature decreases over 5 times from 4.78×10^{-4} Ω m for the undoped sample to 9.25×10^{-5} Ω m for the $AgSb_{0.98}Mg_{0.02}Se_2$ sample and then slightly drops to 8.75×10^{-5} Ω m for the $AgSb_{0.96}Mg_{0.04}Se_2$ sample, resulting from the strongly increased carrier concentration shown in Table 1. As expected, Ba-doped samples exhibit a different variation tendency in comparison with the corresponding Mg-doped samples. As shown in Figure 4b, the electrical resistivity first decreases from 4.78×10^{-4} Ω m for the undoped sample to 1.29×10^{-4} Ω m for the $AgSb_{0.98}Ba_{0.02}Se_2$ sample and then slightly rises to 2.01×10^{-5} Ω m for the $AgSb_{0.96}Ba_{0.04}Se_2$ sample. The difference can primarily be attributed to the presence of $BaSe_3$ nano-precipitates, which results in slight reduction of carrier concentrations and mobility for the $AgSb_{0.96}Ba_{0.04}Se_2$ sample shown in Table 1.

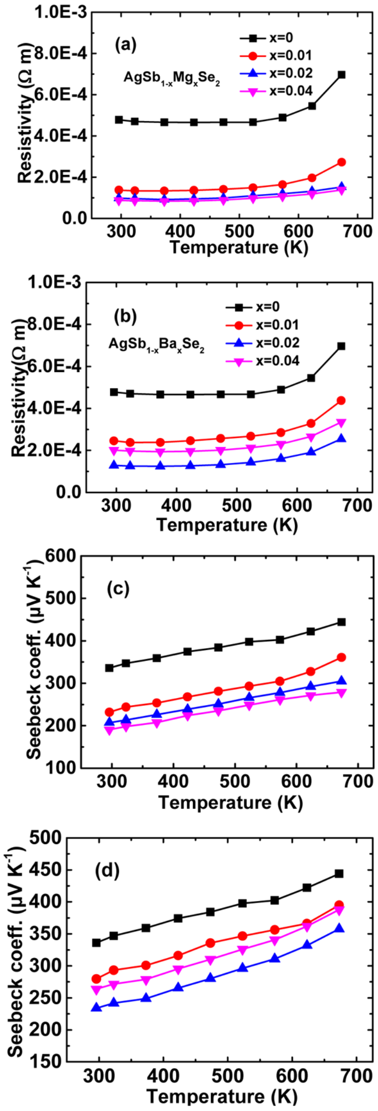

Figure 4. (a) Electrical resistivity for $AgSb_{1-x}Mg_xSe_2$ samples. (b) Electrical resistivity for $AgSb_{1-x}Ba_xSe_2$ samples. (c) Seebeck coefficient for $AgSb_{1-x}Mg_xSe_2$ samples. (d) Seebeck coefficient for $AgSb_{1-x}Ba_xSe_2$ samples.

The temperature-dependent Seebeck coefficient of Mg-doped and Ba-doped $AgSbSe_2$ samples are presented in parts (c) and (d), respectively, of Figure 4. For all the samples, the positive Seebeck coefficients indicate p-type semiconducting nature. The Seebeck coefficients show a gradual decrease with increasing the Mg-doping concentration, while they first decrease and then increase with increasing the Ba-doping concentration, consistent with the tendency of the electrical resistivity. Undoped $AgSbSe_2$ sample exhibits a large Seebeck coefficient ranging from 336 $\mu V\ K^{-1}$ at 300 K to 444 $\mu V\ K^{-1}$ at 673 K, which may be associated with the high effective mass at the Fermi level (m^*). Generally, a rough estimation of the effective mass can be obtained by eqs 1−3 based on the single-band model.[43]

$$m^* = \frac{h^2}{2k_BT}\left[\frac{n}{4\pi F_{1/2}(\eta)}\right]^{2/3} \tag{1}$$

$$S = \pm\frac{k_B}{e}\left[\frac{(r+\frac{5}{2})F_{r+3/2}(\eta)}{(r+\frac{3}{2})F_{r+1/2}(\eta)} - \eta\right] \tag{2}$$

$$F_n(\eta) = \int_0^\infty \frac{\chi^n}{1+e^{\chi-\eta}}\,d\chi \tag{3}$$

where $F_n(\eta)$ is the nth order Fermi integral, η the reduced Fermi energy, r the scattering factor, h the Plank constant, k_B the Boltzmann constant, and e the electron charge. As acoustic phonon scattering is commonly the main scattering mechanism for most thermoelectric materials, the scattering factor r could be considered as $-^1/_2$ in calculation. The obtained effective mass (m^*) for $AgSbSe_2$ is $1.7m_e$, much larger than that of some complex thermoelectric materials, for example, $0.6m_e$ for BiCuSeO[40] and $0.36m_e$ for BiAgSeS.[44] The large effective mass is related to the multiple degenerate valence bands of $AgSbSe_2$.[45] The Pisarenko plot, Seebeck coefficient as a function of carrier concentration, at room temperature is depicted using a simple parabolic band model (SPB) based on eqs 1−3, shown in Figure 5. Obviously, all the doping data in the $AgSbSe_2$ system lay around the Pisarenko plot with effective mass $m^* = 2.0m_0$, which indicate that the diverse doping does not exhibit a significant influence on the band structure of $AgSbSe_2$.

Power factor ($PF = S^2\sigma$) calculated from the measured electrical resistivity and Seebeck coefficient is plotted in Figure 6a,b. Obviously, both Mg doping and Ba doping could significantly enhance the overall power factor. The maximum power factor of Mg- and Ba-doping sample are twice as high as

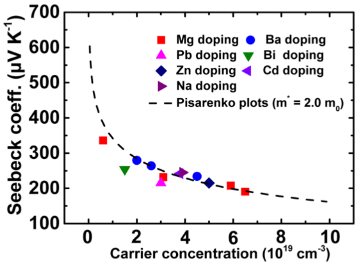

Figure 5. Pisarenko plot with effective mass $m^* = 2.0m_0$ at room temperature, including Mg, Ba, Pb, Bi, Zn, Na, and Cd doping.

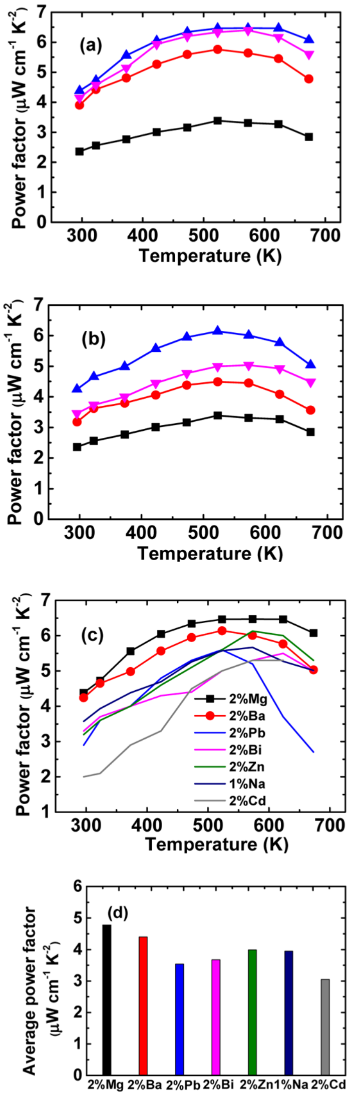

Figure 6. (a) Power factor for $AgSb_{1-x}Mg_xSe_2$ samples. (b) Power factor for $AgSb_{1-x}Ba_xSe_2$ samples. (c) Power factor for $AgSb_{0.98}Mg_{0.02}Se_2$, $AgSb_{0.98}Ba_{0.02}Se_2$, $AgSb_{0.98}Pb_{0.02}Se_2$, $AgSb_{0.98}Bi_{0.02}Se_2$, $AgSb_{0.98}Zn_{0.02}Se_2$, $AgSb_{0.99}Na_{0.01}Se_2$, and $AgSb_{0.98}Cd_{0.02}Se_2$. (d) Average power factor from 300 to 673 K for $AgSb_{0.98}Mg_{0.02}Se_2$, $AgSb_{0.98}Ba_{0.02}Se_2$, $AgSb_{0.98}Pb_{0.02}Se_2$, $AgSb_{0.98}Bi_{0.02}Se_2$, $AgSb_{0.98}Zn_{0.02}Se_2$, $AgSb_{0.99}Na_{0.01}Se_2$, and $AgSb_{0.98}Cd_{0.02}Se_2$.

that of the undoped $AgSbSe_2$ sample, such as 6.5 μW cm^{-1} K^{-2} for the $AgSb_{0.98}Mg_{0.02}Se_2$ sample and 6.1 μW cm^{-1} K^{-2} for the $AgSb_{0.98}Ba_{0.02}Se_2$ sample at 523 K. More significantly, the average power factors in our work, especially for the $AgSb_{0.98}Mg_{0.02}Se_2$ sample, are much higher than that of previously reported results.[26,33−35] Since the power factor determines the output power for given hot and cold temperatures and leg length, as shown by eq 4,[46] it is as important as high ZT values or even more important when the heat source is unlimited (such as solar heat), or the heat source is free (such as waste heat from automobiles, steel industry, etc.) for thermoelectric devices,

$$\omega = \frac{1}{4}\frac{(T_h - T_c)^2}{L}PF \tag{4}$$

where ω, T_h, T_c, and L represent the output power density, hot-side temperature, cold-side temperature, and leg length of thermoelectric modules, respectively. It should be noted that the power factor for $AgSb_{0.98}Mg_{0.02}Se_2$ is still much lower than that of the state-of-the-art thermoelectric materials. Further enhancement could be expected by modulation doping, which have been confirmed in the SiGe,[47] BiCuSeO,[48] and BiAgSeS[49] system.

Parts (a) and (b) of Figure 7 show the total thermal conductivity κ_{total} as a function of temperature for $AgSb_{1-x}Mg_xSe_2$ and $AgSb_{1-x}Ba_xSe_2$ samples, respectively. The

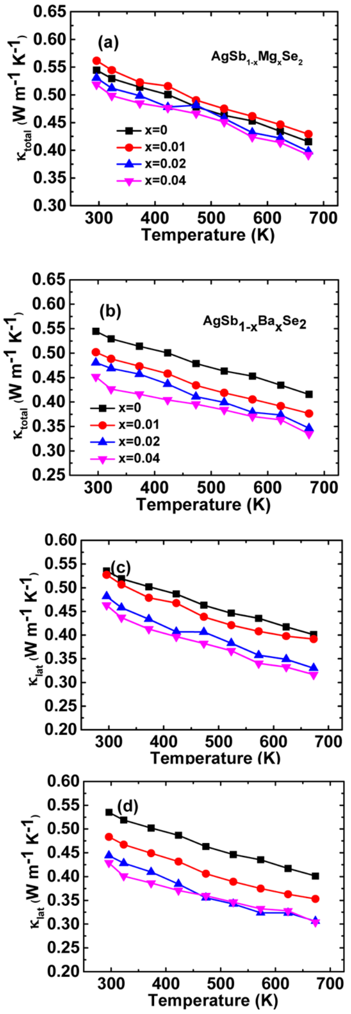

Figure 7. Temperature-dependent thermal transport properties for $AgSb_{1-x}Mg_xSe_2$ and $AgSb_{1-x}Ba_xSe_2$ samples (x = 0, 0.01, 0.02, and 0.04). (a) and (b) Total thermal conductivity κ_{total}. (c) and (d) Lattice thermal conductivity κ_{lat}.

inverse temperature dependence of κ_{total} reveals the predominant phonon contribution to the thermal conductivity. Typically, the κ_{total} of $AgSbSe_2$ deceases from 0.56 to 0.43 W m^{-1} K^{-1} with increasing temperature, even much lower than that of nanostructured $AgPb_mSbTe_{2+m}$ alloys.[10] The intrinsically low thermal conductivity can be ascribed to the disordered Ag and Sb positions and strong bond anharmonicity with a high Grüneisen parameter of ~3.4, which is much higher than that of other I−V−VI_2 compounds, such as $AgBiSe_2$ ~ 2.5 and $AgSbTe_2$ ~ 2.05.[28] The origin of the high Grüneisen parameter is related to the presence of lone s^2 pair electrons of Sb.[20] With increasing Mg-doping concentration, the total thermal conductivity κ_{total} first slightly increases and then decreases in the entire measured temperature range. In contrast, the κ_{total} of Ba-doped samples monotonously reduce with the increase of Ba-doping concentrations. Generally, the κ_{total} consists of two parts, including the lattice thermal conductivity (κ_{lat}) and the electronic thermal conductivity (κ_{ele}). The κ_{lat} can be obtained by directly subtracting κ_{ele} from κ_{total}, in which the κ_{ele} is calculated through the Wiedemann−Franz relationship, $\kappa_{\text{ele}} = L\sigma T$, where L is the Lorenz number. Herein, the Lorenz number L is obtained by fitting the respective Seebeck coefficient with an estimate of the reduced chemical potential using a single parabolic band (SPB) model with acoustic phonon scattering by eqs 2, 3, and 5 rather than using a constant value of 2.45 × 10^{-8} W Ω K^{-2} for degenerate semiconductor, shown in Figure S6.[43]

$$L = \left(\frac{k_B}{e}\right)^2 \left[\frac{3F_2(\eta)}{F_0(\eta)} - \left(\frac{2F_1(\eta)}{F_0(\eta)}\right)^2\right] \tag{5}$$

Therefore, the obtained κ_{lat} of Mg-doped and Ba-doped samples is shown in parts (c) and (d), respectively, of Figure 7. It can be readily observed that the κ_{lat} shows a gradual reduction with increasing Mg- and Ba-doping concentration. Namely, the κ_{lat} at room temperature decreases from 0.54 W m^{-1} K^{-1} for $AgSbSe_2$ to 0.52 W m^{-1} K^{-1} for $AgSb_{0.96}Mg_{0.04}Se_2$ and 0.45 W m^{-1} K^{-1} for $AgSb_{0.96}Ba_{0.04}Se_2$. This variation can be partly explained by the point defects scattering originating from mass and strain field fluctuations caused by the mass and size differences between host atom Sb (121.76 g mol^{-1}, 1.41 Å) and doping atom Mg (24.30 g mol^{-1}, 1.36 Å) and Ba (137.33 g mol^{-1}, 1.98 Å) in the $AgSbSe_2$ solid solution. Indeed, the κ_{lat} of Ba-doped samples exhibit a more obvious suppression than that of Mg doping shown in Figure 7d. For example, the κ_{lat} at room temperature ranges from 0.48 W m^{-1} K^{-1} for $AgSb_{0.99}Ba_{0.01}Se_2$ to 0.43 W m^{-1} K^{-1} for $AgSb_{0.96}Ba_{0.04}Se_2$ at 673 K, which shows ~10% additional reduction in comparison with the κ_{lat} of corresponding Mg-doped samples.

To clarify the contribution of each scattering process to the lattice thermal conductivity, the lattice thermal conductivity of $AgSbSe_2$ can be written using the Debye-Callaway formula,[50]

$$\kappa_L = \frac{k_B}{2\pi^2 v_s}\left(\frac{k_B T}{\hbar}\right)^3 \int_0^{\theta_D/T} \frac{x^4 e^x}{\tau_C^{-1}(e^x - 1)^2}\,dx \tag{6}$$

where x is the reduced frequency ($x = \hbar\omega/k_BT$), ω the phonon angular frequency, k_B the Boltzmann constant, v_s the sound speed, $\hbar$ the reduced Planck constant, θ_D the Debye temperature, and τ_C the combined phonon relaxation time. θ_D and v_s values for $AgSbSe_2$ were used in our fitting and are 143 K and 2454 m/s,[20] respectively.

We consider four different scattering mechanisms in our work, including the point-defects scattering, phonon−phonon scattering, grain boundary scattering, and nanoinclusion (with radius R and volume fraction n) scattering. Therefore, the combined phonon relaxation time can be expressed as

$$\tau_C^{-1} = A\omega^4 + CT\omega^2 + \frac{v_s}{L} + \frac{3}{2}\frac{nv_s}{R} \tag{7}$$

where L is the average grain size ~20 μm and the coefficients A and C are fitting parameters. Since one cannot distinguish the grain boundary scattering from nanoinclusion scattering, it is convenient to define an effective mean free path:

$$\frac{1}{L_{\text{eff}}} = \frac{1}{L} + \frac{3}{2}\frac{n}{R} \tag{8}$$

The value of C depends only on the crystal structure of $AgSbSe_2$. Thus, we obtain the value of C by fitting eq 6 to the lattice thermal conductivity of undoped $AgSbSe_2$. The fitting results are shown as the solid line fits to the experimental data in Figure 8. The coefficients A and L_{eff} for all of these samples are listed in Table 2.

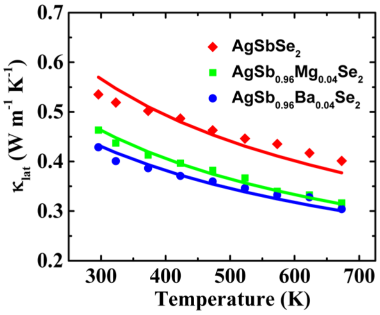

Figure 8. Temperature-dependent lattice thermal conductivity for $AgSbSe_2$, $AgSb_{0.96}Mg_{0.04}Se_2$, and $AgSb_{0.96}Ba_{0.04}Se_2$. The solid lines are the fitting results based on eqs 6−8

Table 2. Values of Lattice Thermal Conductivity Fit Parameters as Defined by eqs 6−8 for $AgSb_{1-x}Mg_xSe_2$ and $AgSb_{1-x}Ba_xSe_2$ Samples

samples	C (10^{-18} s K^{-1})	A (10^{-40} s^3)	L_{eff} (μm)
$AgSbSe_2$	6.03	2.34	21.1
$AgSb_{0.99}Mg_{0.01}Se_2$	6.03	2.54	20.2
$AgSb_{0.98}Mg_{0.02}Se_2$	6.03	3.20	23.1
$AgSb_{0.96}Mg_{0.04}Se_2$	6.03	3.51	22.4
$AgSb_{0.99}Ba_{0.01}Se_2$	6.03	3.02	19.7
$AgSb_{0.98}Ba_{0.02}Se_2$	6.03	3.67	14.6
$AgSb_{0.96}Ba_{0.04}Se_2$	6.03	3.63	8.2

Unexpectedly, very strong point-defects scattering is observed even in the undoped $AgSbSe_2$ sample, consistent with the existence of Ag−Sb disorder. The point-defects scattering rate increase with the increased Mg- or Ba-doping concentration, originating from the mass and strain field fluctuations. Moreover, it can be clearly seen from Table 2 that the L_{eff} values drastically drop with the increased Ba-doping concentration while they are almost unchanged for the Mg-doped samples, in agreement with the different microstructural feature discussed above.

To study the effects of nanoprecipitates on the lattice thermal conductivity of $AgSbSe_2$, we calculate the accumulative lattice thermal conductivity of undoped $AgSbSe_2$, as shown in

Figure 9. It is clear that a large part of heat energy is carried by the mid-to-long-wavelength phonons with mean free path length longer than 50 nm. As short-wavelength phonons could be scattered by the atomic-scale atoms and defects, the remaining mid-to-long-wavelength phonons are highly significant components in thermal conduction. Therefore, the appearance of the $BaSe_3$ nanoprecipitates with the size ranging from 10 to 30 nm could play a critical role in scattering those heat-carrying phonons and then suppress the lattice thermal conductivity, as demonstrated in the current work. Coupled with the atomic-scale point defects and mesoscale grain boundary, this all-scale hierarchical scattering architecture in the Ba-doped $AgSbSe_2$ results in the ultralow lattice thermal conductivity, κ_{lat}, as low as 0.3 W m^{-1} K^{-1} at 673 K for $AgSb_{0.98}Ba_{0.02}Se_2$.

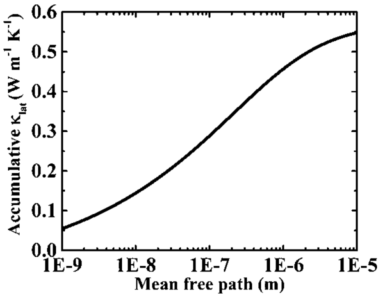

Figure 9. Accumulative lattice thermal conductivity as a function of mean free path for undoped $AgSbSe_2$ at 300 K.

With combing of the electrical and thermal properties of Mg-doped and Ba-doped $AgSbSe_2$ samples, the corresponding *ZT* values are shown in parts (a) and (b), respectively, of Figure 10. The synergistic combination of the improved power factor and the reduced thermal conductivity contributes to an enhanced *ZT* value for the alkaline-earth metal ions (Mg^{2+} and Ba^{2+}) doping. A high *ZT* ∼ 1 is obtained for $AgSb_{0.98}Mg_{0.02}Se_2$ and $AgSb_{0.98}Ba_{0.02}Se_2$ samples at 673 K, which is increased by around a factor of 2 compared with that of undoped $AgSbSe_2$. Moreover, it is highly expected that higher *ZT* values could be achieved by modulation doping to enhance the power factor. The thermoelectric efficiency was calculated using the method proposed by Kim et al. under the consideration of the Thomson effect.[51] This method can more accurately and reliably predict the maximum efficiency by accounting for a cumulative temperature dependence of S, ρ, and κ regarding a single homogeneous TE leg under ideal conditions. The results shown in Figure 10c demonstrate that alkaline-earth metal ions (Mg^{2+} and Ba^{2+}) doping will significantly enhance the leg efficiency of $AgSbSe_2$ for nearly 80%. More importantly, the highest leg efficiency for $AgSb_{0.98}Mg_{0.02}Se_2$ and $AgSb_{0.98}Ba_{0.02}Se_2$ samples are 8.43% and 8.58% with T_c = 300 K and T_h = 673 K, respectively, which demonstrates that the $AgSbSe_2$ system is a robust Te-free candidate for medium-temperature power generation applications.

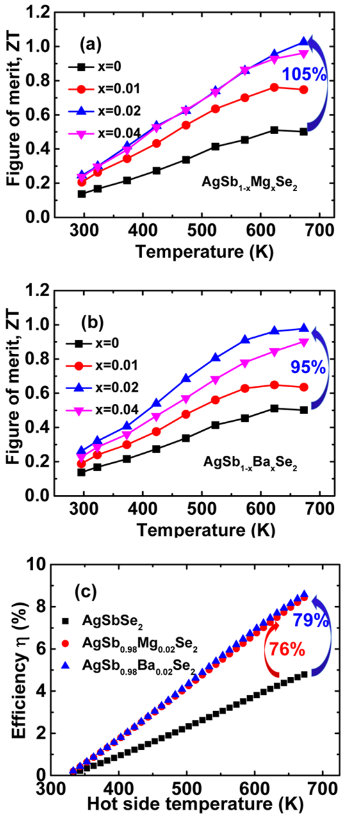

Figure 10. (a) and (b) Temperature-dependent *ZT* values for $AgSb_{1-x}Mg_xSe_2$ and $AgSb_{1-x}Ba_xSe_2$ samples (x = 0, 0.01, 0.02, and 0.04). (c) Calculated leg efficiency of $AgSbSe_2$, $AgSb_{0.98}Mg_{0.02}Se_2$, and $AgSb_{0.98}Ba_{0.02}Se_2$ with T_c = 300 K and T_h = 673 K.

4. CONCLUSION

In summary, the microstructure and thermoelectric properties of alkaline-earth metal ions (Mg^{2+} and Ba^{2+}) doping in the $AgSbSe_2$ system are investigated. Mg^{2+} doping merely optimizes the carrier concentration and thus significantly enhances the power factor. Meanwhile, the lattice thermal conductivity is gradually reduced by strong point defects scattering. In comparison, Ba^{2+} doping not only increases the carrier concentration but also interestingly generates large amounts of nanoprecipitates in the $AgSbSe_2$ matrix, contributing to the obvious suppression of total thermal conductivity. A high *ZT* ∼ 1 at 673 K and leg efficiency ∼8.5% with T_c = 300 K and T_h = 673 K for $AgSb_{0.98}Mg_{0.02}Se_2$ and $AgSb_{0.98}Ba_{0.02}Se_2$ samples are achieved, which indicate the $AgSbSe_2$ system is a robust Te-free candidate for medium-temperature power generation applications. Furthermore, the enhancement of the *ZT* value could be achieved by modulation doping to simultaneously increase the carrier concentration and mobility.

■ ASSOCIATED CONTENT

Ⓢ Supporting Information

Thermal diffusivity, heat capacity, XRD patterns, backscattering SEM image, element distribution map, and the calculated Lorenz number, Figure S1−S6. The Supporting Information is available free of charge on the ACS Publications website at DOI: 10.1021/acsami.5b06492.

■ AUTHOR INFORMATION

Corresponding Authors

*E-mail: weicai@hit.edu.cn.
*E-mail: suijiehe@hit.edu.cn.

Notes

The authors declare no competing financial interest.

ACKNOWLEDGMENTS

This work was supported by the National Natural Science Foundation of China (no. 51471061 and 51271069 8) and by the Program for New Century Excellent Talents in University of Ministry of Education of China (NCET-12-0160) (J.S.).

REFERENCES

(1) Rowe, D. M. *CRC Handbook of Thermoelectrics*; CRC Press: Boca Raton, FL, 1995.

(2) Yang, J.; Caillat, T. Thermoelectric Materials for Space and Automotive Power Generation. *MRS Bull.* **2006**, *31*, 224−229.

(3) Goldsmid, H. J. *Introduction to Thermoelectricity*; Springer: Heidelberg, 2009.

(4) Snyder, G. J.; Toberer, E. S. Complex Thermoelectric Materials. *Nat. Mater.* **2008**, *7*, 105−114.

(5) Liu, W. S.; Yan, X.; Chen, G.; Ren, Z. F. Recent Advances in Thermoelectric Nanocomposites. *Nano Energy* **2012**, *1*, 42−56.

(6) Pei, Y. Z.; Wang, H.; Snyder, G. J. Band Engineering of Thermoelectric Materials. *Adv. Mater.* **2012**, *24*, 6125−6135.

(7) Heremans, J. P.; Jovovic, V.; Toberer, E. S.; Saramat, A.; Kurosaki, K.; Charoenphakdee, A.; Yamanaka, S.; Snyder, G. J. Enhancement of Thermoelectric Efficiency in PbTe by Distortion of the Electronic Density of States. *Science* **2008**, *321*, 554−557.

(8) Pei, Y. Z.; Shi, X. Y.; LaLonde, A.; Wang, H.; Chen, L. D.; Snyder, G. J. Convergence of Electronic Bands for High Performance Bulk Thermoelectrics. *Nature* **2011**, *473*, 66−69.

(9) Kim, W.; Zide, J.; Gossard, A.; Klenov, D.; Stemmer, S.; Shakouri, A.; Majumdar, A. Thermal Conductivity Reduction and Thermoelectric Figure of Merit Increase by Embedding Nanoparticles in Crystalline Semiconductors. *Phys. Rev. Lett.* **2006**, *96*, 045901.

(10) Hsu, K. F.; Loo, S.; Guo, F.; Chen, W.; Dyck, J. S.; Uher, C.; Hogan, T.; Polychroniadis, E. K.; Kanatzidis, M. G. Cubic $AgPb_mSbTe_{2+m}$: Bulk Thermoelectric Materials with High Figure of Merit. *Science* **2004**, *303*, 818−821.

(11) Liu, Z. H.; Pei, Y. L.; Geng, H. Y.; Zhou, J. C.; Meng, X. F.; Cai, W.; Liu, W. S.; Sui, J. H. Enhanced Thermoelectric Performance of Bi_2S_3 by Synergistical Action of Bromine Substitution and Copper Nanoparticles. *Nano Energy* **2015**, *13*, 554−562.

(12) Poudel, B.; Hao, Q.; Ma, Y.; Lan, Y. C.; Minnich, A.; Yu, B.; Yan, X. A.; Wang, D. Z.; Muto, A.; Vashaee, D.; Chen, X. Y.; Liu, J. M.; Dresselhaus, M. S.; Chen, G.; Ren, Z. F. High-Thermoelectric Performance of Nanostructured Bismuth Antimony Telluride Bulk Alloys. *Science* **2008**, *320*, 634−638.

(13) Biswas, K.; He, J. Q.; Blum, I. D.; Wu, C. I.; Hogan, T. P.; Seidman, D. N.; Dravid, V. P.; Kanatzidis, M. G. High-Performance Bulk Thermoelectrics with All-Scale Hierarchical Architectures. *Nature* **2012**, *489*, 414−418.

(14) Zhao, L. D.; Dravid, V. P.; Kanatzidis, M. G. The Panoscopic Approach to High Performance Thermoelectrics. *Energy Environ. Sci.* **2014**, *7*, 251−268.

(15) He, J. Q.; Kanatzidis, M. G.; Dravid, V. P. High Performance Bulk Thermoelectrics via a Panoscopic Approach. *Mater. Today* **2013**, *16*, 166−176.

(16) Zhang, X.; Zhao, L. D. Thermoelectric Materials: Energy Conversion between Heat and Electricity. *Journal of Materiomics* **2015**, *1*, 92−105.

(17) Brown, S. R.; Kauzlarich, S. M.; Gascoin, F.; Snyder, G. J. $Yb_{14}MnSb_{11}$: New High Efficiency Thermoelectric Material for Power Generation. *Chem. Mater.* **2006**, *18*, 1873−1877.

(18) Snyder, G. J.; Christensen, M.; Nishibori, E.; Caillat, T.; Iversen, B. B. Disordered Zinc in Zn_4Sb_3 with Phonon-Glass and Electron-Crystal Thermoelectric Properties. *Nat. Mater.* **2004**, *3*, 458−463.

(19) Christensen, M.; Abrahamsen, A. B.; Christensen, N. B.; Juranyi, F.; Andersen, N. H.; Lefmann, K.; Andreasson, J.; Bahl, C. R. H.; Iversen, B. B. Avoided Crossing of Rattler Modes in Thermoelectric Materials. *Nat. Mater.* **2008**, *7*, 811−815.

(20) Nielsen, M. D.; Ozolins, V.; Heremans, J. P. Lone Pair Electrons Minimize Lattice Thermal Conductivity. *Energy Environ. Sci.* **2013**, *6*, 570−578.

(21) Liu, H.; Shi, X.; Xu, F.; Zhang, L.; Zhang, W.; Chen, L. D.; Li, Q.; Uher, C.; Day, T.; Snyder, G. J. Copper Ion Liquid-Like Thermoelectrics. *Nat. Mater.* **2012**, *11*, 422−425.

(22) He, Y.; Day, T.; Zhang, T. S.; Liu, H. L.; Shi, X.; Chen, L. D.; Snyder, G. J. High Thermoelectric Performance in Non-Toxic Earth-Abundant Copper Sulfide. *Adv. Mater.* **2014**, *26*, 3974−3978.

(23) Zhao, L. D.; Lo, S. H.; Zhang, Y.; Sun, H.; Tan, G.; Uher, C.; Wolverton, C.; Dravid, V. P.; Kanatzidis, M. G. Ultralow Thermal Conductivity and High Thermoelectric Figure of Merit in SnSe Crystals. *Nature* **2014**, *508*, 373−377.

(24) Wang, H.; Li, J. F.; Zou, M.; Sui, T. Synthesis and Transport Property of $AgSbTe_2$ as a Promising Thermoelectric Compound. *Appl. Phys. Lett.* **2008**, *93*, 202106.

(25) Jovovic, V.; Heremans, J. P. Doping Effects on the Thermoelectric Properties of $AgSbTe_2$. *J. Electron. Mater.* **2009**, *38*, 1504−1509.

(26) Guin, S. N.; Chatterjee, A.; Negi, D. S.; Datta, R.; Biswas, K. High Thermoelectric Performance in Tellurium Free p-Type $AgSbSe_2$. *Energy Environ. Sci.* **2013**, *6*, 2603−2608.

(27) Guin, S. N.; Biswas, K. Cation Disorder and Bond Anharmonicity Optimize the Thermoelectric Properties in Kinetically Stabilized Rocksalt $AgBiS_2$ Nanocrystals. *Chem. Mater.* **2013**, *25*, 3225−3231.

(28) Morelli, D. T.; Jovovic, V.; Heremans, J. P. Intrinsically Minimal Thermal Conductivity in Cubic I-V-VI_2 Semiconductors. *Phys. Rev. Lett.* **2008**, *101*, 035901.

(29) Amatya, R.; Ram, R. J. Trend for Thermoelectric Materials and Their Earth Abundance. *J. Electron. Mater.* **2012**, *41*, 1011−1019.

(30) Pan, L.; Berardan, D.; Dragoe, N. High Thermoelectric Properties of n-Type $AgBiSe_2$. *J. Am. Chem. Soc.* **2013**, *135*, 4914−4917.

(31) Guin, S. N.; Srihari, V.; Biswas, K. Promising Thermoelectric Performance in n-Type $AgBiSe_2$: Effect of Aliovalent Anion Doping. *J. Mater. Chem. A* **2015**, *3*, 648−655.

(32) Xiao, C.; Xu, J.; Cao, B.; Li, K.; Kong, M.; Xie, Y. Solid-Solutioned Homojunction Nanoplates with Disordered Lattice: A Promising Approach toward "Phonon Glass Electron Crystal" Thermoelectric Materials. *J. Am. Chem. Soc.* **2012**, *134*, 7971−7977.

(33) Guin, S. N.; Negi, D. S.; Datta, R.; Biswas, K. Nanostructuring, Carrier Engineering and Bond Anharmonicity Synergistically Boost the Thermoelectric Performance of p-Type $AgSbSe_2$-ZnSe. *J. Mater. Chem. A* **2014**, *2*, 4324−4331.

(34) Guin, S. N.; Chatterjee, A.; Biswas, K. Enhanced Thermoelectric Performance in p-Type $AgSbSe_2$ by Cd-Doping. *RSC Adv.* **2014**, *4*, 11811−11815.

(35) Cai, S. T.; Liu, Z. H.; Sun, J. Y.; Li, R.; Fei, W. D.; Sui, J. Enhancement of Thermoelectric Properties by Na Doping in Te-Free p-Type $AgSbSe_2$. *Dalton Trans.* **2015**, *44*, 1046−1051.

(36) Guin, S. N.; Biswas, K. Sb Deficiencies Control Hole Transport and Boost the Thermoelectric Performance of p-Type $AgSbSe_2$. *J. Mater. Chem. C* **2015**, DOI: 10.1039/C5TC01429H.

(37) Zhao, L. D.; Wu, H. J.; Hao, S. Q.; Wu, C. I.; Zhou, X. Y.; Biswas, K.; He, J. Q.; Hogan, T. P.; Uher, C.; Wolverton, C.; Dravid, V. P.; Kanatzidis, M. G. All-Scale Hierarchical Thermoelectrics: MgTe in PbTe Facilitates Valence Band Convergence and Suppresses Bipolar Thermal Transport for High Performance. *Energy Environ. Sci.* **2013**, *6*, 3346−3355.

(38) Biswas, K.; He, J. Q.; Wang, G. Y.; Lo, S. H.; Uher, C.; Dravid, V. P.; Kanatzidis, M. G. High Thermoelectric Figure of Merit in Nanostructured p-Type PbTe−MTe (M= Ca, Ba). *Energy Environ. Sci.* **2011**, *4*, 4675−4684.

(39) Wang, H.; Gibbs, Z. M.; Takagiwa, Y.; Snyder, G. J. Tuning Bands of PbSe for Better Thermoelectric Efficiency. *Energy Environ. Sci.* **2014**, *7*, 804−811.

(40) Li, J.; Sui, J. H.; Pei, Y. L.; Barreteau, C.; Berardan, D.; Dragoe, N.; Cai, W.; He, J. Q.; Zhao, L. D. A High Thermoelectric Figure of

Merit ZT > 1 in Ba Heavily Doped BiCuSeO Oxyselenides. *Energy Environ. Sci.* **2012**, *5*, 8543−8547.

(41) Pei, Y. L.; He, J. Q.; Li, J. F.; Li, F.; Liu, Q. J.; Pan, W.; Barreteau, C.; Berardan, D.; Dragoe, N.; Zhao, L. D. High Thermoelectric Performance of Oxyselenides: Intrinsically Low Thermal Conductivity of Ca-Doped BiCuSeO. *NPG Asia Mater.* **2013**, *5*, e47.

(42) Barreteau, C.; Berardan, D.; Amzallag, E.; Zhao, L. D.; Dragoe, N. Structural and Electronic Transport Properties in Sr-Doped BiCuSeO. *Chem. Mater.* **2012**, *24*, 3168−3178.

(43) Zhao, L. D.; Lo, S. H.; He, J. Q.; Li, H.; Biswas, K.; Androulakis, J.; Wu, C. I.; Hogan, T. P.; Chung, D. Y.; Dravid, V. P.; Kanatzidis, M. G. High Performance Thermoelectrics from Earth-Abundant Materials: Enhanced Figure of Merit in PbS by Second Phase Nanostructures. *J. Am. Chem. Soc.* **2011**, *133*, 20476−20487.

(44) Pei, Y. L.; Wu, H. J.; Sui, J. H.; Li, J.; Berardan, D.; Barreteau, C.; Pan, L.; Dragoe, N.; Liu, W. S.; He, J. Q.; Zhao, L. D. High Thermoelectric Performance in n-Type BiAgSeS Due to Intrinsically Low Thermal Conductivity. *Energy Environ. Sci.* **2013**, *6*, 1750−1755.

(45) Hoang, K.; Mahanti, S. D.; Salvador, J. R.; Kanatzidis, M. G. Atomic Ordering and Gap Formation in Ag-Sb-Based Ternary Chalcogenides. *Phys. Rev. Lett.* **2007**, *99*, 156403.

(46) Liu, W. S.; Jie, Q.; Kim, H. S.; Ren, Z. F. Current Progress and Future Challenges in Thermoelectric Power Generation: From Materials to Devices. *Acta Mater.* **2015**, *87*, 357−376.

(47) Zebarjadi, M.; Joshi, G.; Zhu, G. H.; Yu, B.; Minnich, A.; Lan, Y. C.; Wang, X. W.; Dresselhaus, M.; Ren, Z. F.; Chen, G. Power Factor Enhancement by Modulation Doping in Bulk Nanocomposites. *Nano Lett.* **2011**, *11*, 2225−2230.

(48) Pei, Y. L.; Wu, H. J.; Wu, D.; Zheng, F. S.; He, J. Q. High Thermoelectric Performance Realized in a BiCuSeO System by Improving Carrier Mobility through 3D Modulation Doping. *J. Am. Chem. Soc.* **2014**, *136*, 13902−13908.

(49) Wu, D.; Pei, Y. L.; Wang, Z.; Wu, H. J.; Huang, L.; Zhao, L. D.; He, J. Q. Significantly Enhanced Thermoelectric Performance in n-Type Heterogeneous BiAgSeS Composites. *Adv. Funct. Mater.* **2014**, *24*, 7763−7771.

(50) Callaway, J. Model for Lattice Thermal Conductivity at Low Temperatures. *Phys. Rev.* **1959**, *113*, 1046.

(51) Kim, H. S.; Liu, W. S.; Chen, G.; Chu, C. W.; Ren, Z. F. Relationship between Thermoelectric Figure of Merit and Energy Conversion Efficiency. *Proc. Natl. Acad. Sci. U. S. A.* **2015**, *112*, 8205−8210.